Malekan, Mohammad; Khosravi, Ali; Zhao, Xiaowei

The Influence of Magnetic Field on Heat Transfer of Magnetic Nanofluid in a Double Pipe Heat Exchanger Proposed in a Small-Scale CAES System

Published in:
Applied Thermal Engineering

DOI:
10.1016/j.applthermaleng.2018.09.117

Published: 05/01/2019

Document Version
Peer-reviewed accepted author manuscript, also known as Final accepted manuscript or Post-print

The Influence of Magnetic Field on Heat Transfer of Magnetic Nanofluid in a Double Pipe Heat Exchanger Proposed in a Small-Scale CAES System

Mohammad Malekan [1], Ali Khosravi [2*], Xiaowei Zhao[3]

[1] Department of Bioengineering, Heart Institute (InCor), Medical School, University of São Paulo, Brazil

[2] Department of Mechanical Engineering, School of Engineering, Aalto University, Finland
School of Engineering, The University of Warwick, United Kingdom

* Corresponding author: Ali.khosravi@aalto.fi, Alikhosravii@yahoo.com

Abstract

Globally, the integration of renewable energy (which has an intermittent nature) into the power system requires the system operators to improve the system performance to be able to effectively handle the variations of the power production in order to balance the supply and demand. This problem is seen as a major obstacle to the expansion of renewable energy if it is not handled in a suitable way. Efficient electricity storage technology is one of the feasible solutions. The current study proposes Fe_3O_4/water nanofluid under magnetic field as the secondary fluid in the proposed double pipe heat exchanger before the cavern. The heat of compressed air is absorbed by the secondary fluid and it is stored in an isolation tank. This stored fluid is used to warm up the air that leaves the cavern for expanding in the turbine. The results demonstrated that increasing the mass flow rate of secondary fluid decreases the cavern temperature. Also, the value of convective heat transfer of ferrofluid increases when the volume fraction of nanoparticle as well as magnetic field increases. Furthermore, increasing the volume fraction and magnetic field increases the pressure drop and friction factor of ferrofluid.

Keywords: Magnetic field; Compressed air energy storage; Ferrofluid; Transient response; Fe_3O_4 nanoparticles

1. Introduction

Renewable energy sources (such as solar, wind, ocean thermal, geothermal, etc.) are extensively available and have a potential to meet the energy demand of the whole mankind [1], [2]. However, harnessing of these renewable energy sources for energy production units is not a simple process, due to several reasons including intermittency, changing weather condition, time, and geographical location. One solution to this problem is to introduce energy storage systems such as compressed air energy storage (CAES), hydrogen storage system, battery, etc. [3]. CAES is an alternative to pumped hydro, since it has relatively high power output and storage capacity. Instead of pumping water to an upper reservoir when the electricity supply is high, atmospheric air is compressed and stored in underground facilities under high pressure in CAES system [4]. When the demand for electricity is high, the stored air is heated and expanded through a generator to produce electricity [5].

There are currently two CAES plants in operation worldwide. The first one was installed in Huntorf, Germany in 1978 and the second one, located in McIntosch-USA, was put into operation in 1991. Both systems compress air adiabatically and use the natural gas as heat sources for discharge process. Many investigations have been developed recently to improve CAES system [6], [7]. Szablowski et al. [8] constructed a dynamic mathematical model of an adiabatic CAES system using Aspen Hysys software. The volume of cavern for the studied CAES system was considered as 310,000 m^3. Also, the operation pressure inside the cavern changed from 43 to 70 bar. Their results

demonstrated that the maximum exergy destruction was occurred in the compressor and turbine. Wang and Bauer [9] analyzed the pressure response of large-scale CAES system in porous formations. The developed model showed that the induced pressure changed laterally throughout the storage formation was due to initial filling of the air storage. Houssainy et al. [10] implemented a thermodynamic analysis of a high-temperature hybrid CAES system. They have showed the importance of thermal storage temperature and pressure on the system. An optimum operating pressure was proposed in order to obtain the maximum roundtrip storage efficiency of the proposed hybrid storage system.

For an adiabatic CAES system, a novel throttling strategy (by considering an internal ejector) was proposed by Chen et al. [11]. For this new system, the internal ejector increases the inlet pressure of high-pressure turbine that can lead to increasing in the system efficiency. In addition, their results have demonstrated that employing the internal ejector can increase the roundtrip efficiency approximately by 2%. An accurate prediction of the energy storage capacity of a cavern with a defined storage volume and type is the first step of planning and designing a CAES system. According to this, for a large-scale CAES system, a study was developed by He et al. [12] to analyze the exergy storage of compressed air in cavern and cavern volume prediction. Techno-economic modeling of a large-scale CAES system was implemented by Huang et al. [13]. Two types of CAES systems including adiabatic one and conventional one were modeled using ECLIPSE software. Their overall obtained efficiencies were 64.7% and 52.6%, respectively.

Mazloum et al. [14] performed an exergy analysis and exergo-economic optimization of a constant-pressure isobaric adiabatic CAES system. A steady-state model was developed to evaluate the CAES system, which has an efficiency of around 55%. In addition, an optimization method based on genetic algorithm was employed to optimize the system. By applying this optimization method, they improved the efficiency of the CAES system by 2.7%. Kim and Kim [15] evaluated the effect of steam injection in a CAES system, which showed that the electricity generation of the steam injection was approximately 7% more than the conventional system. Alami et al. [16] proposed a low pressure, modular CAES system for wind energy storage applications. In another study, Meng et al. [17] proposed a CAES system integrated with an organic Rankine cycle that was evaluated from energy and economic point of views.

In a diabatic CAES system, the air heat up and is stored as compressed air in a cavern. During discharging, the air cools down due to its expansion and has to be heated up by burning conventional fuel or biofuel. The current study proposes a double pipe heat exchanger with a ferrofluid as secondary fluid before cavern absorbs the heat of compressed air in charging stage and warm up the air in discharge stage. Ferrofluid, with a size of 5–15nm in diameter, which is composed of magnetic nanoparticles such as nickel, iron, cobalt and their oxides is able to improve the heat transfer coefficient in the presence of magnetic field [18]. Heat exchangers are applied to various engineering systems such as food industry, power generation, heat recovery systems, and process plants [19]. Many investigations have been developed to assess the effect of magnetic field on heat transfer of nanofluids. Naphon and Wiriyasart [20] developed an experimental study on laminar pulsating flow and heat transfer of nanofluids in micro-fins tube with magnetic fields. The experiment conditions were: Reynolds number varied from 1000 to 2400;

volume fractions of nanoparticles in the base fluid were 0.25% and 0.5%; the inlet temperature of nanofluid was 20℃. It was concluded that the pulsating flow and magnetic field have an advantage on the Brownian motion of nanoparticles in the base fluid. Moreover, the pulsating frequency, magnetic field strength, and nanoparticle concentration increase the heat transfer rate. Zonouzi et al. [21] evaluated the flow and magnetic nanofluid in a vertical tube under magnetic quadrupole field. Their experimental results have illustrated that the local heat transfer coefficient was increased by 23.4%, 37.9% and 48.9% for 2 vol% Fe_3O_4 in the presence of the quadrupole magnets located at three different axial installation positions.

Computational approaches, such as computational fluid dynamics (CFD), are very useful to investigate the HTC for different engineering problems [22]–[24]. Mousavi et al. [19] implemented a CFD study to assess the influence of magnetic field on heat transfer of magnetic Fe_3O_4/water nanofluid (4 vol. %) in a sinusoidal double pipe heat exchanger. It was observed that sinusoidal formation of the internal tube as well as magnetic field significantly increases the Nusselt number. Sheikholeslami et al. [25] investigated the effect of magnetic nanofluid (CuO/water) in a permeable channel via Lattice Boltzmann method. They reported that the heat transfer rate rises with an increase of permeability of porous medium. In addition, temperature boundary layer thickness enhances in the presence of the magnetic field. Gan Jia Gui et al. [26] performed an experimental investigation to evaluate the effect of external magnetic field on heat transfer enhancement of nanofluids. It was concluded that the convective heat transfer of nanofluid improved by increasing the solid volume concentration of magnetic nanoparticles (0.2 to 0.4%). They reported that increasing the magnetic flux decreased the heat transfer enhancement.

Hosseini et al. [27] investigated the nanofluid (Al_2O_3/water) heat transfer in a microchannel heat sink under the effect of magnetic field using KKL model. They reported a direct relationship between Nusselt number and magnetic field. Malekan and Khosravi [18] developed a study based on CFD simulation and adaptive neuro-fuzzy inference system optimized with particle swarm optimization to assess the effect of magnetic field on heat transfer of Fe_3O_4/water nanofluid in a tube. It was achieved that the heat transfer of nanofluid at presence of magnetic field increases. Also, the developed intelligent model successfully predicted the heat transfer coefficient of magnetic nanofluid with different intensity of magnetic field. Also, several investigations (numerical and experimental) have been developed to evaluate the effect of magnetic field on heat transfer enhancement of nanofluids: Naphon and Wiriyasart [28] investigated pulsating flow and magnetic field effects on heat transfer enhancement of TiO_2/water nanofluid in helically corrugated tube. Sandeep and Animasaun [29] evaluated the effect of magnetic field on heat transfer improvement of magnetic nanofluids in a wall jet flow. Hatami et al. [30] assessed the effect of magnetic field on nanofluids heat transfer through a uniformly heated horizontal tube. Sha et al. [31] conducted an experimental investigation to analyze the influence of magnetic field on convective heat transfer of Fe_3O_4/water nanofluid. Hariri et al [32] and Mokhtari et al. [33] were analyzed the effects of magnetic field on ferrofluid performance in tubes without and with twisted tapes. Khosravi et al. [34], [35] have investigated the ferrofluid characteristics and its heat transfer properties in the presence of magnetic field for in tube for different industrial applications. And more recently, Sheikholeslami et al. [36] evaluated the influence of non-uniform magnetic field on heat transfer enhancement of ferrofluid in a 90° elbow channel.

Based on the literature many investigations were developed to improve CAES system. In this study, for the first time, a double pipe heat exchanger with Fe_3O_4/water nanofluid (as secondary fluid) under magnetic field is proposed for a CAES system. For this target, a transient model is developed to analyze the CAES system (the compression process) and also a computational fluid dynamics (CFD) simulation is employed to assess the magnetic nanofluid as secondary fluid in the heat exchanger. The developed transient model is fed only with the temperature and pressure at the compressor inlet (these input parameters are coming from the environment). The ferrofluid is considered with different volume fractions. The numerical simulation is executed using the capabilities of CFD approach embedded in ANSYS Fluent 18.2.

2. The proposed model

The main advantage of implementing a CAES system is considering it as an ancillary service for a grid. Applications include: spinning reserve, peak shaving, VAR (voltage-ampere reactive) support and arbitrage. The compressed air energy storage (CAES) system involves the excess available energy to compress the ambient air to a strong pressure of approximately 70 bar. This excess available energy commonly produces by renewable energy systems such as photovoltaic system and wind turbine. The first step is to compress the ambient air by a series of compressors. And then, the high pressure air is stored in a cavern. This compressed air is expanded through a conventional gas turbine in order to provide the required electricity when the demand of electricity is high [37]. To insure the maximum energy is obtained, during the expansion process, some additional energy such as natural gas is used. During compression, heat is generated which is removed before stored. This process is done by applying a double pipe heat exchanger before the cavern. Figure 1 indicates the proposed CAES system with a double pipe heat exchanger, which uses from Fe_3O_4/water nanofluid under magnetic field as secondary fluid. This study concentrates on the compression of air.

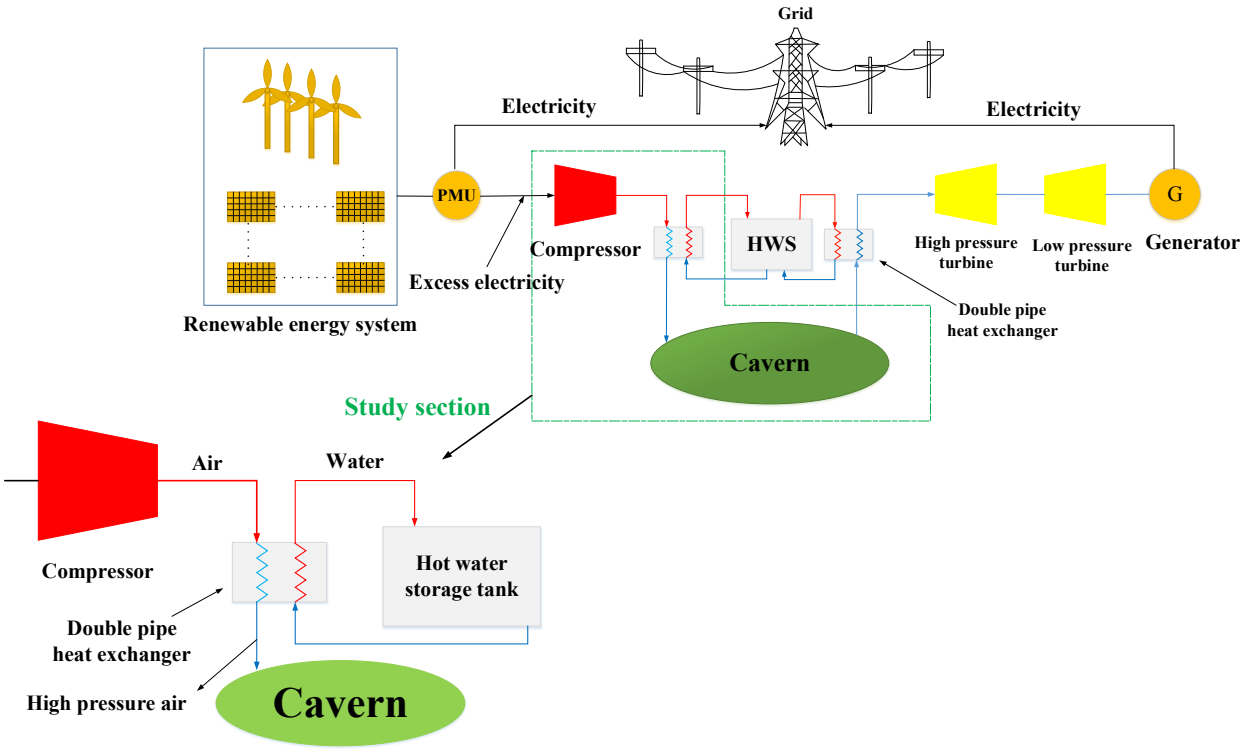

Fig. 1. Schematic diagram of the proposed system.

Figure 2 shows the schematic of the heat exchanger geometry along with its dimensions and mesh discretization scheme. The magnetic field is generated by current-carrying wire located in the position (a, b) parallel to the tube longitudinal axis z, below the outer tube wall (see Fig. 2(a)). The current-carrying wire causes a non-uniform transverse magnetic field perpendicular to the ferrofluid flow direction. The effects of this magnetic field on hydro-thermal characteristics of the magnetic nanofluid are investigated by applying a single phase model.

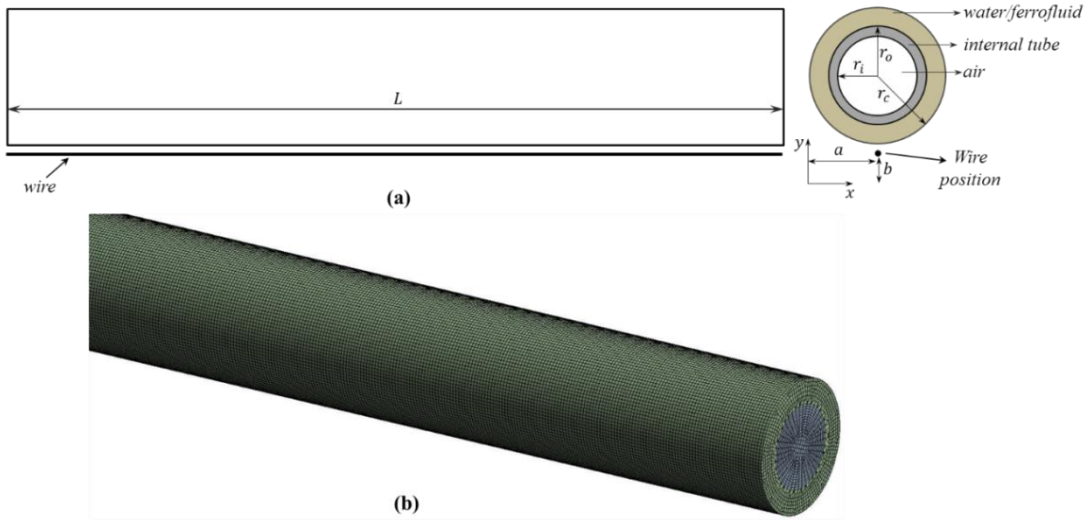

Fig. 2. (a) Geometry of the problem, with $= 3\ m, r_i = 5.35\ mm, r_o = 6.35\ mm, r_c = a = 8.525\ mm, b = 1\ mm$, and (b) cell discretization schematic.

3. Mathematical Modeling

3.1. Ferrofluid Thermo-Physical Properties

Thermo-physical properties of the ferrofluid (ff) depend on the volumetric fraction (φ) and physical properties of the nanoparticles (p) as well as the base fluid (f). Ferrofluid density, specific heat capacity, thermal conductivity, and dynamic viscosity are calculated by:

$$\rho_{ff} = (1-\varphi)\rho_f + \varphi\rho_p \quad (1)$$

$$C_{p,ff} = (1-\varphi)C_{p,f} + \varphi C_{p,p} \quad (2)$$

$$\mu_{ff} = (1+2.5\varphi)\mu_f \quad (3)$$

$$k_{ff} = \left(\frac{k_p + (n-1)k_f - (n-1)\varphi(k_f - k_p)}{k_p + (n-1)k_f + \varphi(k_f - k_p)}\right)k_f \quad (4)$$

where ρ is the density, C_p is the specific heat, μ is the dynamic viscosity and k is the thermal conductivity. Subscript ff in Eqs. (1-4) stands for the ferronfluid. Equation (4) was presented for the first time by Hamilton & Crossor [38], and n is the shape factor which is 3 for spherical particles.

In this study, a mixture of water and Fe_3O_4 nanoparticles compounds the ferrofluid, with the different volumetric fractions, with a general volume fraction range of 0.1– 4% [39]. The nanoparticles are spherical with a diameter of about 10 nm. Table 1 presents the properties of the nanoparticles, base fluid, air and the ferrofluid.

Table 1. Thermo-physical properties of materials.

Material	$\rho\ (kg/m^3)$	$C_p\ (J/kg.K)$	$k\ (W/m.K)$	$\mu\ (kg/m.s)$
Air	1.225	1006.43	0.0242	0.000018
Water (base fluid)	998.2	4182	0.6	0.00103
Fe_3O_4 (particle)	5200	670	6	---
Ferrofluid with 2 vol %	1081.84	4109.36	0.63591	0.001082
Ferrofluid with 4 vol %	1165.47	4036.72	0.67328	0.001133

3.2. Heat Transfer Formulations

The convection heat transfer coefficient (h) in theory is calculated by the Nusselt number (Nu). The Nu depends on the flow conditions and the geometry of the problem [40] which is defined by:

$$Nu = \frac{hD_i}{k} \quad (5)$$

By having the pressure drop along the absorber tube, the friction factor (f) can be calculated according to the following relation [41]:

$$f = \frac{2\Delta P}{\rho_{ff}u^2}\left(\frac{D_i}{L}\right) \quad (6)$$

where ΔP is the pressure drop, L is the tube length, and u is the fluid velocity. The theoretical value for the friction factor can be calculated using the Petukhov relation, as [42]:

$$f = (0.79 \cdot \ln Re - 1.64)^{-2} \quad (7)$$

The mathematical model was developed to simulate the dynamic behavior of the CAES. To simulate this behavior, the model was divided into 3 small models (compressor, cavern, and heat exchanger model) (Fig. 3). The following

section describes these three components. The model simulations lead to conclusions about the dynamic behavior of the CAES in different operating conditions.

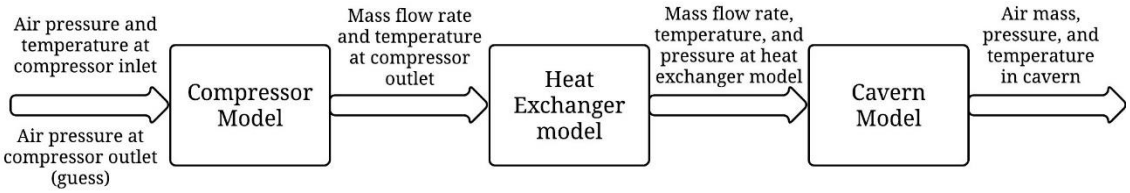

Fig. 3. Flowchart with input and output data in each model.

3.3. Compressor model

The volumetric efficiency of a compressor (η_v) is defined by the ratio of the mass flow real aspirated and the maximum mass flow rate that could be vacuumed. Its theoretical value can be obtained from the thermodynamic cycle of the compressor by the expression:

$$\eta_v = 1 + c - c.\left(\frac{P_{f3}}{P_{f1}}\right)^{\frac{c_v}{c_p}} \tag{8}$$

The variables, c, P_{f3}, P_{f1}, c_v and c_p, respectively represent the dead space coefficient of the compressor, the pressure of condensation and evaporation, the specific heat of the air at constant volume and specific heat of the air at the constant pressure.

Finally, in order to calculate the mass flow in the compressor discharge ($\dot{m}$), the following equation can be used:

$$\dot{m} = N\, V_d\, \rho_1\, \eta_v \tag{9}$$

In which N is the rotational speed of the compressor, V_d is the piston displacement volume, ρ_1 is the specific mass at the compressor inlet and η_v is the volumetric efficiency of the compressor.

3.4. Heat exchanger model

The mathematical modeling of the heat exchanger for water and air fluids is done by considering the mass, energy, and momentum conservation laws simultaneously. The energy conservation law for the air is given by the following equation [43]. The indices j and i represent the control volume position in the heat exchanger composition.

$$\frac{\partial G_f}{\partial z} = -\left(\frac{\rho_f - \rho_f^0}{\Delta t}\right) \tag{10}$$

$$\frac{\partial P_f}{\partial z} = -\left(\frac{G_f - G_f^0}{\Delta t}\right) - \left(\frac{dP}{dz}\right)_f - g\rho_f \sin\theta \tag{11}$$

$$\frac{\partial h_f}{\partial z} = \frac{1}{G_f}\left[\frac{P_f - P_f^0}{\Delta t} - \frac{h_f - h_f^0}{\Delta t}\rho_f + \frac{H_i pe}{A_i}\left(T_t - T_f\right)\right] \tag{12}$$

where $\partial G_f/\partial z$, $\partial P_f/\partial z$, and $\partial h_f/\partial z$ represent the gradient of mass velocity, pressure and specific enthalpy inside the control volume i, ρ is the density, T is the temperature, P is the pressure, t is the time, pe is the perimeter and A is the area. The subscript f stands for air and subscript t stands for tube is the area. The internal convective coefficient

(H_i) which corresponds to the convective coefficient water flow is found according to the Bergman et al. [44] methodology. A cross-section of the heat exchanger is shown in Fig. 4.

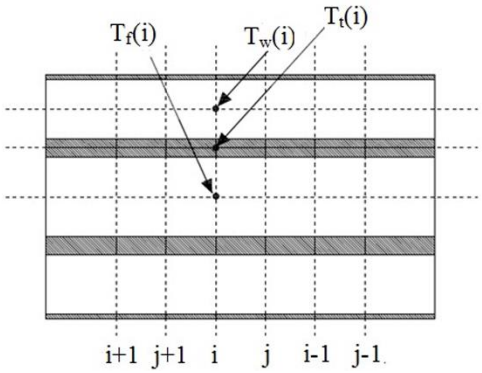

Fig. 4. Cross-section of heat exchanger showing control volumes for the air, tube wall and water.

In addition, the energy balance equations for the water and the heat exchanger wall are as follows [45]:

$$\rho_w A_e cp_w \frac{T_w(i) - T_w^0(i)}{\Delta t} = -G_w A_e cp_w \frac{T_w(j-1) - T_w(j)}{\Delta z} - H_e pe_e \left(T_w - T_t\right) \tag{13}$$

$$\rho_t A_e cp_t \frac{T_t(i) - T_t^0(i)}{\Delta t} = -G_w A_e cp_w \frac{\partial T_w}{\partial z} - H_e pe_e \left(T_w - T_t\right) \tag{14}$$

Where the subscript w refers to water and t refers to the external side of the tube.

3.5. Cavern Model

With the assumption of mass flow remains constant for an instant Δt, the air pressure in the cave (P_c) can be calculated. Using ideal gas equation of state, the pressure in the cave can be determined from

$$P_c = \rho_c R T_c \tag{15}$$

where ρ_c,T_c and R are the density, temperature and gas constant of the air in the cave, respectively. The air temperature in the cave for a given instant of time is calculated by averaging the air temperature in the cave at the previous instant and the temperature of the air at the outlet of the heat exchanger.

$$T_c = \frac{T^0 m^0 + T_{he} m_{he}}{m^0 + m_{he}} \tag{16}$$

where superscript 0 refers to an earlier time step and the subscript he refers to the values at the output of the heat exchanger. Figure 5 shows the flow diagram of the model in order to predict the transient response of small-scale CAES system.

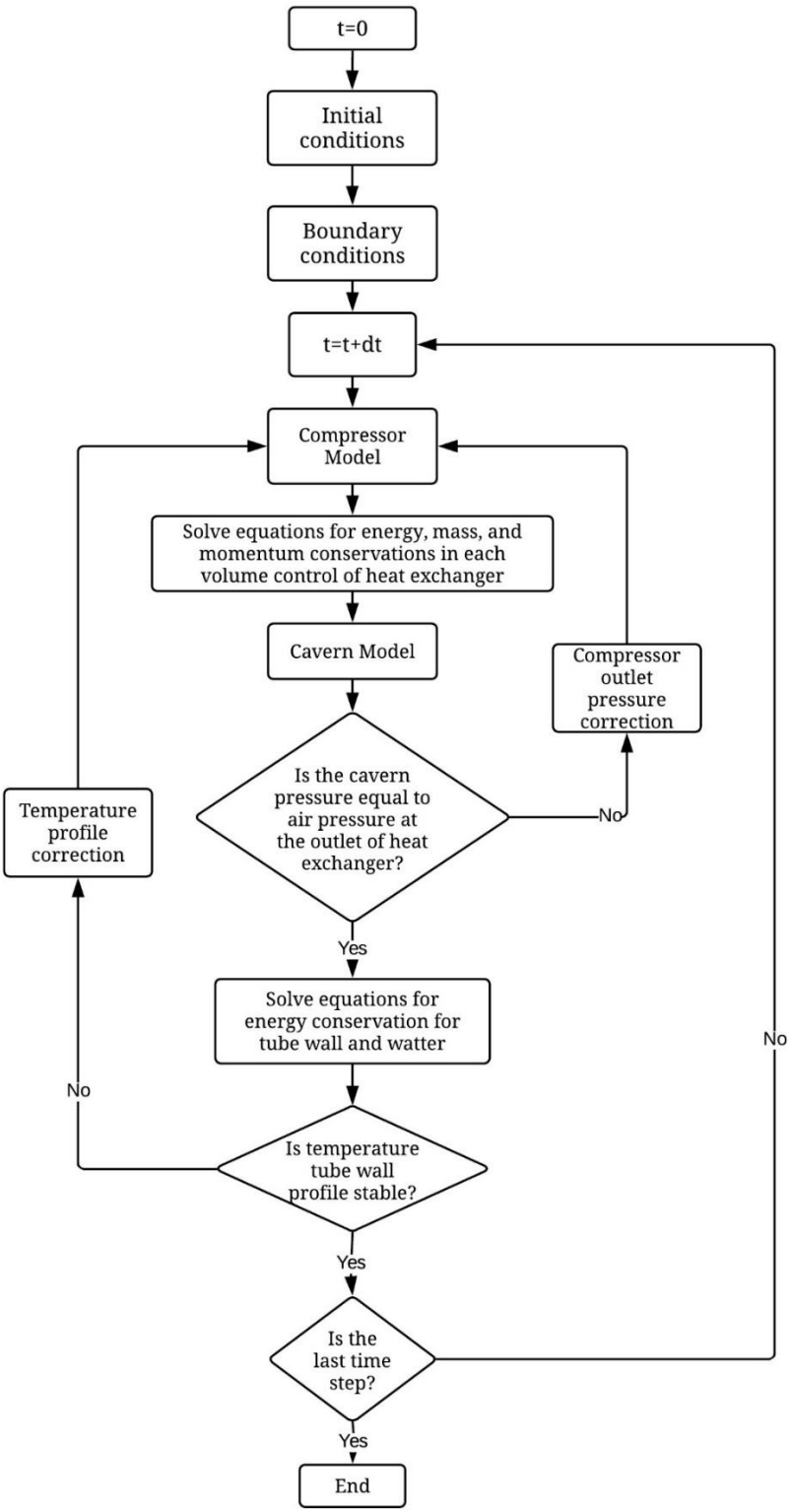

Fig. 5. Flow diagram illustrating the operation of the model.

3.6. Assumptions used

The following assumptions are considered for developing the model:

1. The heat exchanger piping and cavern are considered as perfectly isolated.
2. The properties of the fluids and the wall of the exchanger are considered uniform within a cross-section of the exchanger.
3. Conduction of heat in the radial direction within the wall of the tubes is fast enough to ensure that the inner and outer walls of the inner tube are always at the same temperature.
4. The air and water flows are unidirectional.
5. The potential energy variation of fluids is negligible.

Table 2 represents technical specification of the proposed model.

Table 2. Considered values for the proposed CAES system.

	Parameters	***Values***
Ambient conditions	Ambient temperature (℃)	25
	Ambient pressure (kPa)	91
Compressor	Frequency of the electrical grid (Hz)	60
	Number of poles	2
	Rotation (rpm)	3600
	Cylinder capacity (cm^3)	200
	Isentropic performance	80%
	Coefficient of dead space	10%
Cavern	Cavern volume (L)	100
Heat exchanger	Length (m)	3
	external diameter of the outer tube (inches)	$^3/_4$
	external diameter of the inner tube (inches)	$^1/_2$
	pipe thickness (mm)	1
	Mass flow rate (kg/h)	60
Simulation	Time steps (s)	1
	Total time of simulation (s)	1600
	tolerance for temperature convergence (℃)	1
	tolerance for pressure convergence (Pa)	10

4. Result and discussion

Technical specification of this CAES system is different with the available CAES systems in Huntorf and McIntosh power plants. Hence, the experimental data for this CAES system are not available. A double heat exchanger configuration was investigated by applying a transient model. A prototype of this transient model for the first time was developed by Machado et al. [46], which was employed in several investigations [43], [47]–[49]. For the proposed heat exchanger, located before the cavern, Fe_3O_4/water ferrofluid was proposed as the secondary fluid,

which absorbs the heat of the air before cavern and stores in an isolation tank. This thermal process was simulated by the commercial software ANSYS® Fluent® 18.2. A 3D steady state turbulent k–ε RNG model (with around 5 million of cells) along with standard wall functions and SIMPLEC solution algorithm [50] are used to simulate the heat transfer in the heat exchanger. The second order upwind differencing scheme is used for momentum and energy equations. The convergence limits are set to be equal to 10^{-3} for momentum and mass and 10^{-6} for energy equations. Velocity (varies for hot and cold fluids) and zero pressure is considered for inlet and outlet boundary conditions for both cold and hot fluids. In addition, inlet and outlet temperature for both hot and cold fluid are defined, according to transient model outputs.

4.1. Validity Study

Friction factor is chosen in order to perform validity analysis. Theoretical values from Eq. (7) and numerical results obtained by the simulation calculated using Eq. (6), by having the pressure drop and velocity for each case, are compared to show the validity of the current numerical simulations. As it can be seen from Fig. 6, the present CFD results agree well with the theoretical outputs, with a maximum error of 10% for both air and water tubes.

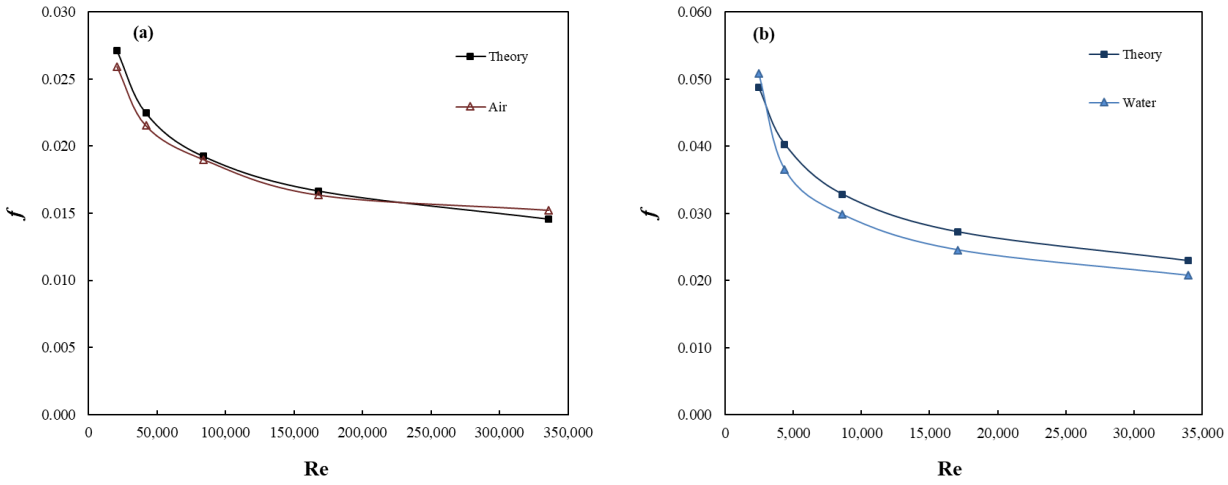

Fig. 6. Friction factor variation to validate the present CFD model with Petukhov correlations [42], (a) air, and (b) water.

4.2. Simulation Results

This section contains numerical results of in-house transient code and steady-state CFD model. The transient model is used mainly to obtain the boundary conditions for the CFD model as well as to obtain a feasible length for the heat exchanger. In the transient model, the range of temperature and pressure of air were initially considered from 81 to 2000 kPa and from 273.15 to 522.15 K, respectively. As can be seen in Fig. 7, the results demonstrate that the temperature and pressure for air during the simulation reach values outside of the initial range. This simulation was developed to determine the optimum range of temperature and pressure for air. As a result, a large range of temperature (from 250 to 1249 K) and pressure (80 to 3500 kPa) was considered to cover the developed equations.

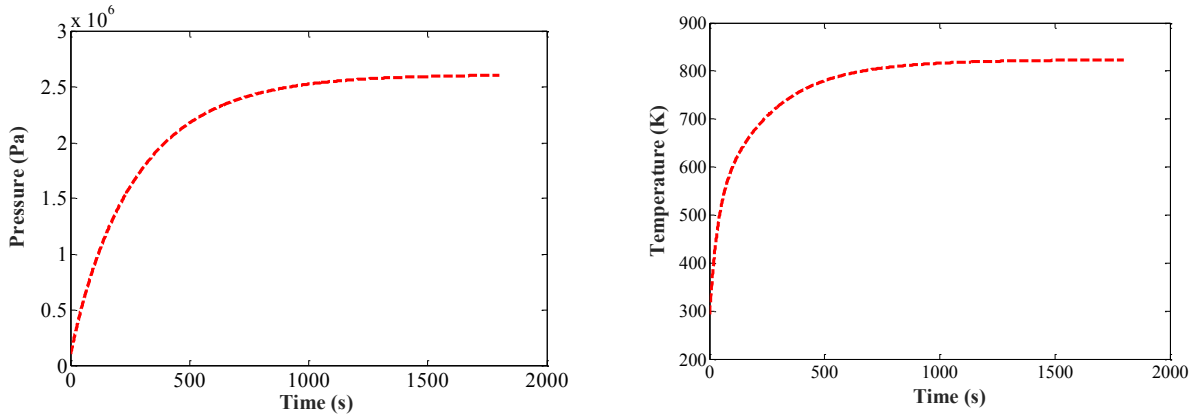

Fig. 7. Preliminary simulation of the evolution of air pressure in the cavern during its filling and air temperature at the compressor outlet during the filling of the cavern.

Fig. 8 shows the variation of the air temperature that calculated by different divisions per meter of the pipe versus the length of exchanger (3 m). The simulation time of this analysis is 100, 400, 1000 and 1600 seconds. As expected, the graph demonstrates that the temperature of air along the length of exchanger decreases from 600 to 300 K (after 100 s). Regarding the figure, after 1000 second, the air temperature inside the heat exchanger reaches approximately 820 K and in the outside of the heat exchanger, it reaches to 300 K.

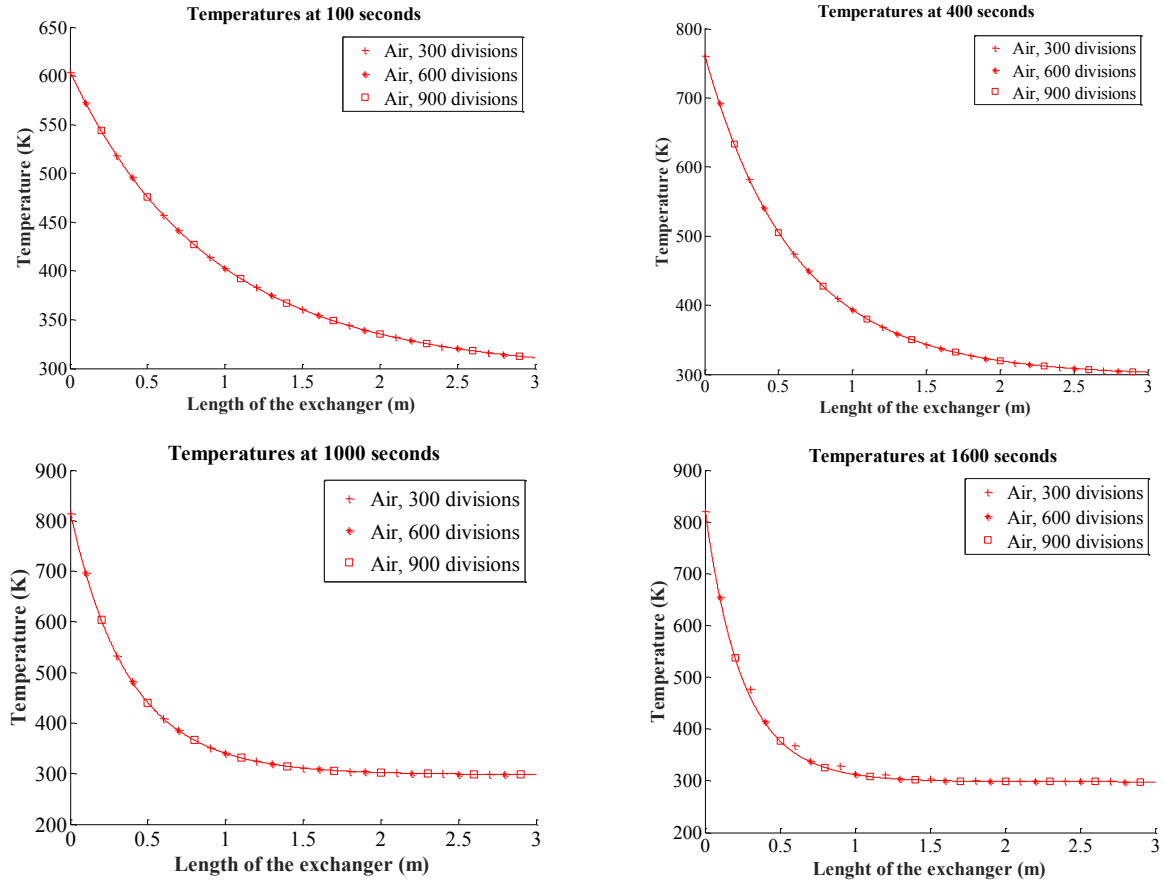

Fig. 8. Preliminary simulation of the evolution of air pressure in the cavern during its filling and air temperature at the compressor outlet during the filling of the cavern.

Figure 9 shows the cavern temperature versus time that was calculated with different values of divisions per meter of the pipe of heat exchanger. The pipe is divided into 300, 600 and 900 sections that the graph illustrates the obtained values are similar for each division per meter of the pipe. The simulation time for this investigation is 1600s in which temperature of the cavern increases from 298 to 308 K, between 0 and 200s time span, and subsequently decreases (from 308 to 306 K) and reaches to a fairly constant value (between 200 and 1600s).

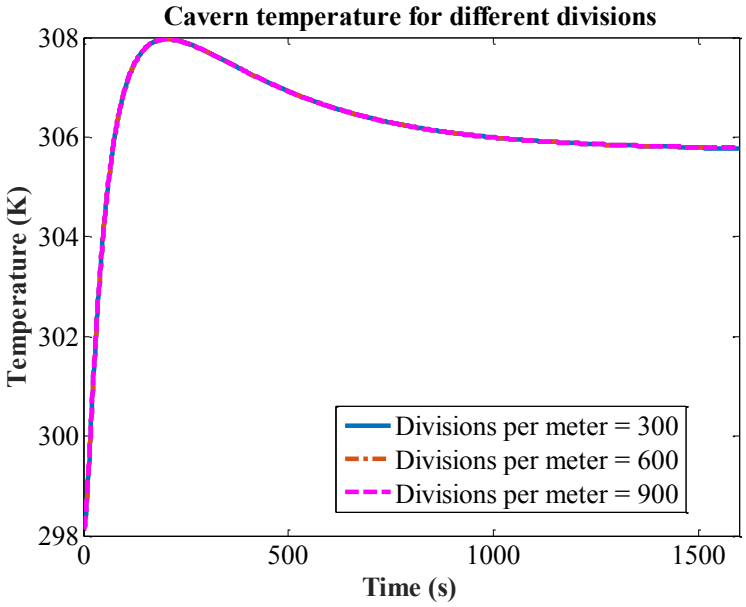

Fig. 9. Variation of cavern temperature calculated with different values of divisions per meter of pipe in the exchanger.

Fig. 10 indicates the cavern temperature values for different mass flow rate of water in the heat exchanger. The graph shows when the mass flow rate of water increases the value of the cavern temperature decreases. The cavern temperature with 30 kg/h water flow in exchanger is approximately 2.3% higher compared to water flow of 100 kg/h.

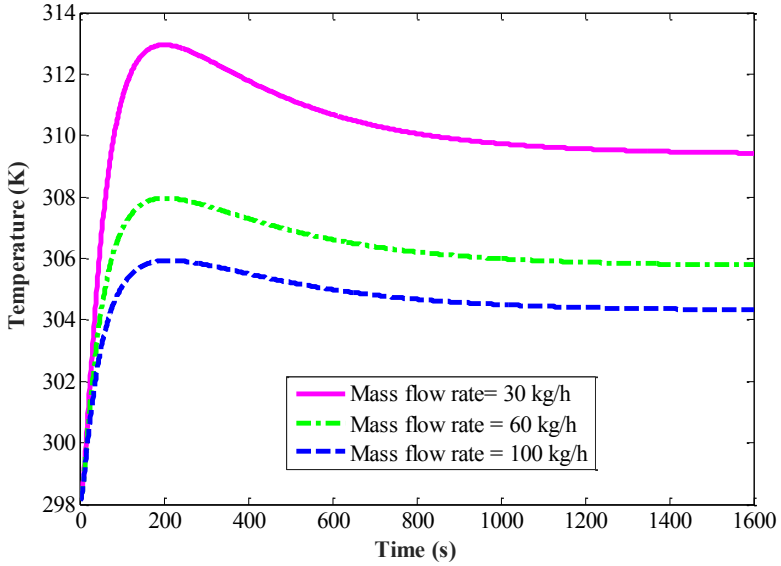

Fig. 10. Cavern temperature values for different water flows.

The length variation of the heat exchanger is considered from 1 to 6 m and the effect of this variation is evaluated for the CAES system. Fig. 11 shows that the variation of the cavern temperature with the length of 1m of heat exchanger is greater than other lengths. In general, the cavern temperature is fairly steady for bigger lengths of heat exchanger.

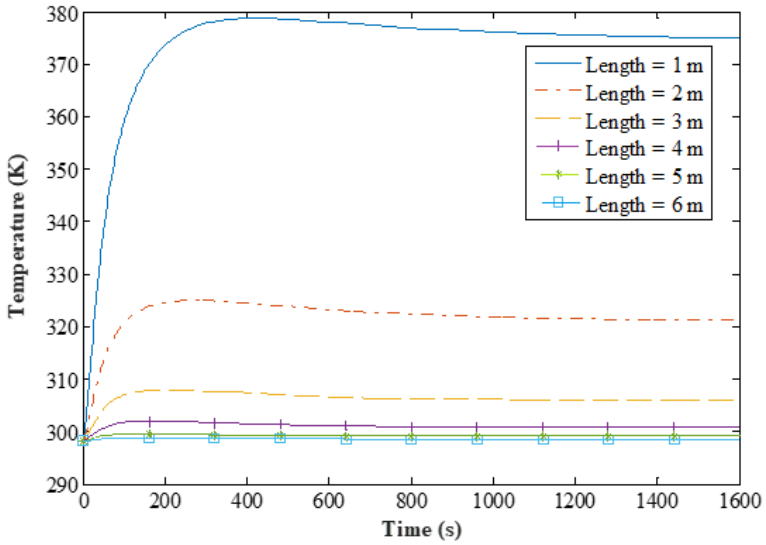

Fig. 11. Cave temperature values for different sizes of the exchanger

According to before mentioned transient model results, temperature for the hot inlet and cold inlet are considered as 800 K and 300 K, respectively. In addition, the length of heat exchanger is considered equal to 2 m. Ferrofluid with different volume fraction (2% and 4%) along with base fluid (water) are used as the cold working fluid, while air is used as the hot working fluid. In addition, a current-carrying wire is located close to the outer tube in order to provide magnetic field for the Fe_3O_4 nanoparticles. Figure 12 presents inlet and outlet temperature and velocity for

the water and air for $Re_{air} = 42{,}000$ and $Re_{water} = 4500$. As it can be seen from this figure, there are a uniform distribution for both temperature and velocity at the inlet and outlet as well. The hot fluid temperature decreased to 433 K, while cold fluid temperature increased up to 325 K.

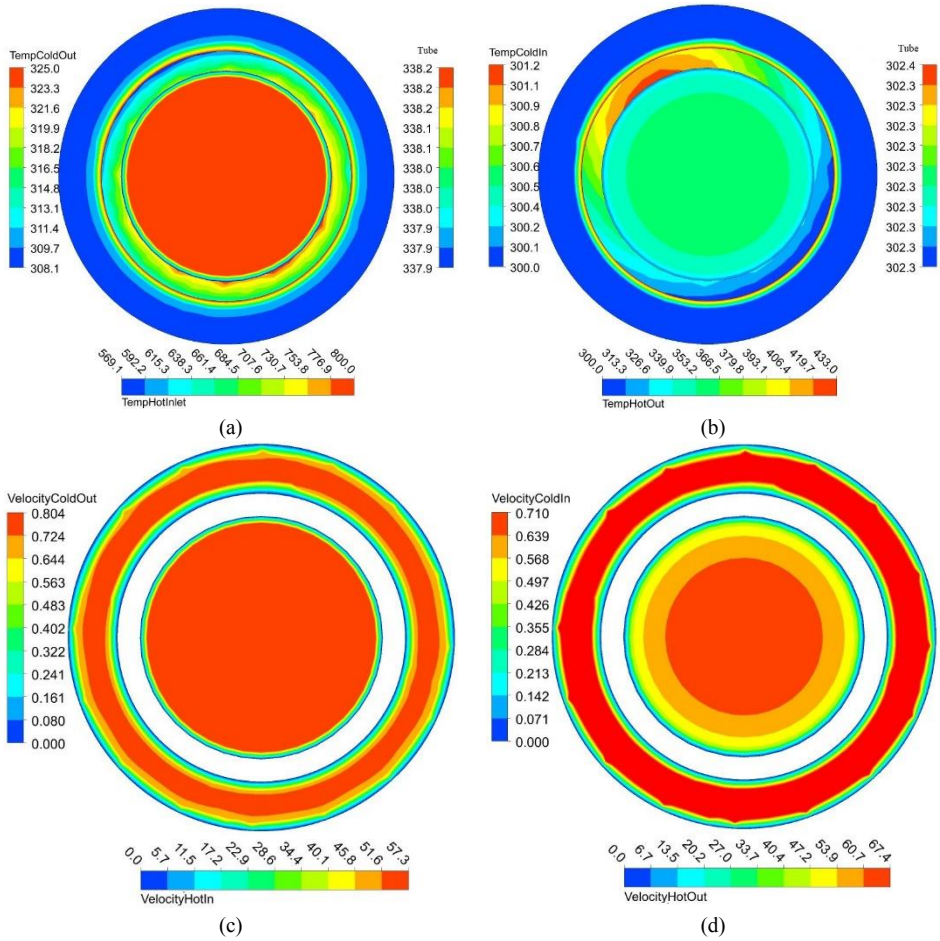

Fig. 12. (a) Temperature (in K) for air inlet and water outlet, (b) Temperature (in K) for air outlet and water inlet, (c) Velocity for air inlet and water outlet, and (d) Velocity for air outlet and water inlet. For $Re_{air} = 42{,}000$ and $Re_{water} = 4500$.

Figures 13 to 16 present inlet and outlet temperature and velocity for air and ferrofluid with different volume fractions with and without presence of magnetic fields (B = 0 and 400 G), for $Re_{air} = 42{,}000$ and $Re_{ff} = 4500$. Comparing Figures 13(a) with 14(a) shows clearly the effect of magnetic field. In addition, looking at Figures 13(a) and 16(a) shows the influence of bigger ferrofluid volume fraction. This helps to have more fraction of the fluid flowing with the maximum temperature. Moreover, magnetic field causes ferrofluid to flow with higher temperature but more concentrated around the inner tube. Also, the magnetic field increases the velocity of the ferrofluid, as it can be seen in Figures 14(c) and 16(c), similar to the results which were presented in [18], [34].

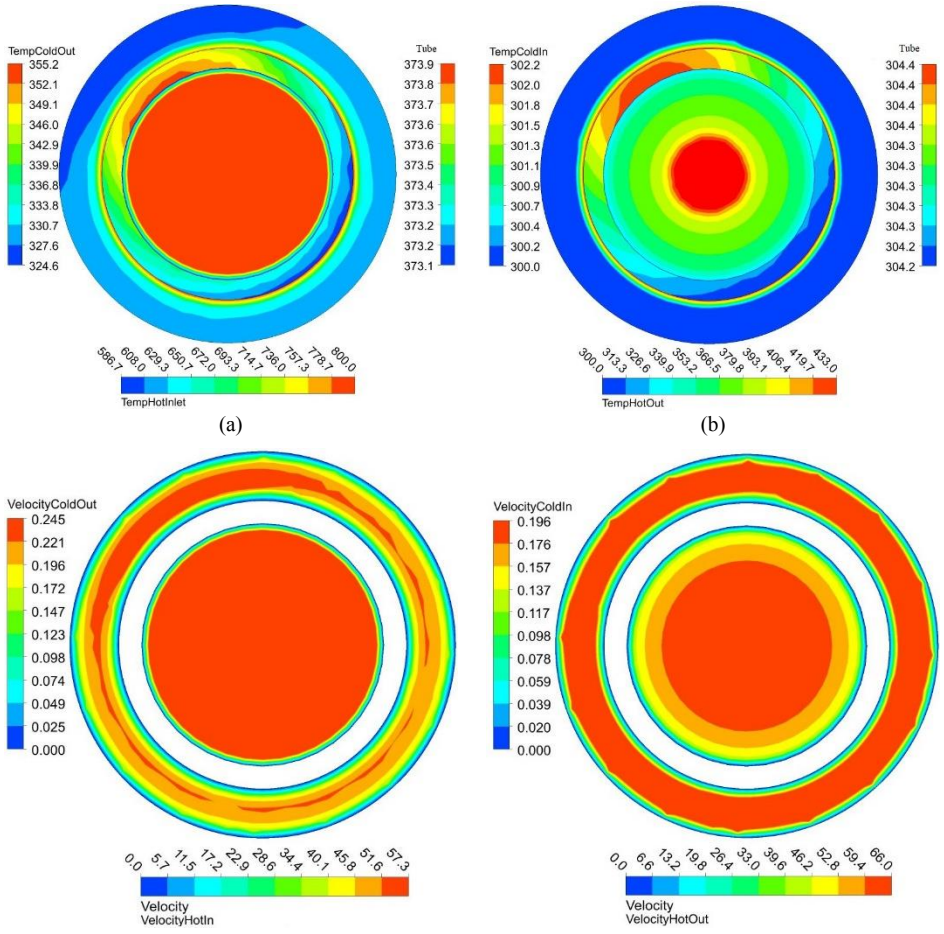

Fig. 13. Ferrofluid with 2 Vol% and without magnetic field: (a) Temperature (in K) for air inlet and water outlet, (b) Temperature (in K) for air outlet and water inlet, (c) Velocity for air inlet and water outlet, and (d) Velocity for air outlet and water inlet. For $Re_{air} = 42{,}000$ and $Re_{water} = 4500$.

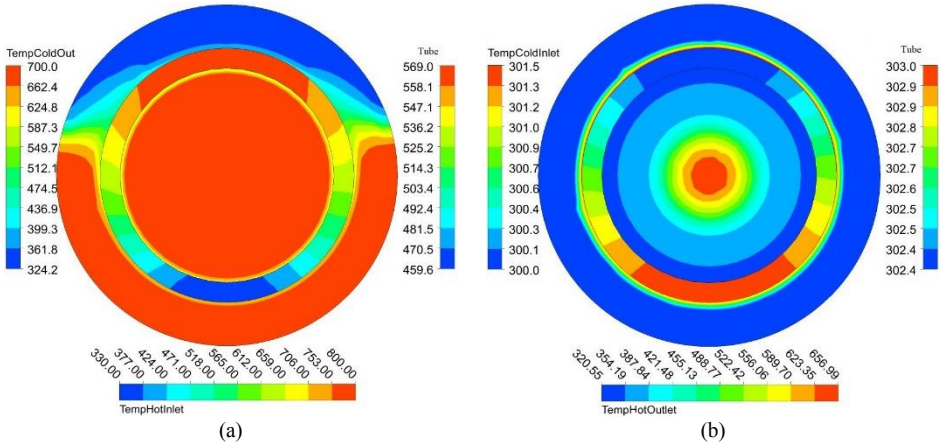

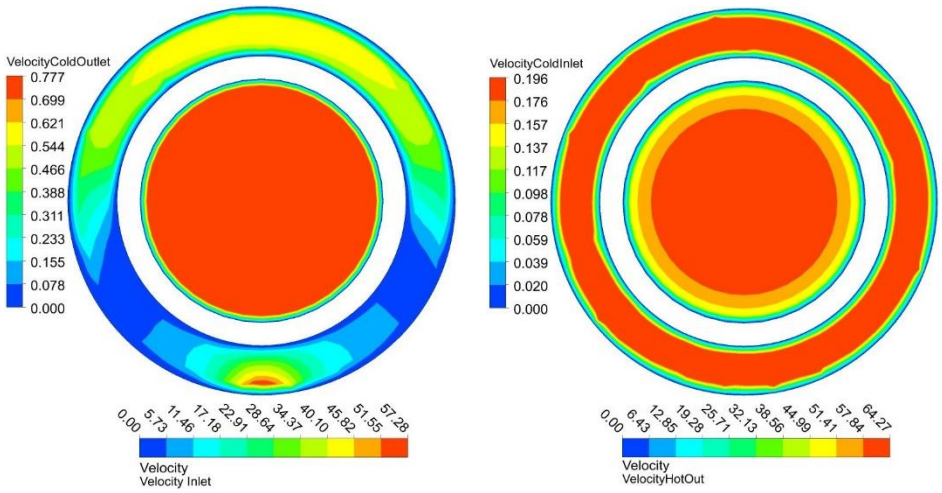

(c) (d)

Fig. 14. Ferrofluid with 2 Vol% and with magnetic field of B = 400 G: (a) Temperature (in K) for air inlet and water outlet, (b) Temperature (in K) for air outlet and water inlet, (c) Velocity for air inlet and water outlet, and (d) Velocity for air outlet and water inlet. For $Re_{air} = 42{,}000$ and $Re_{water} = 4500$.

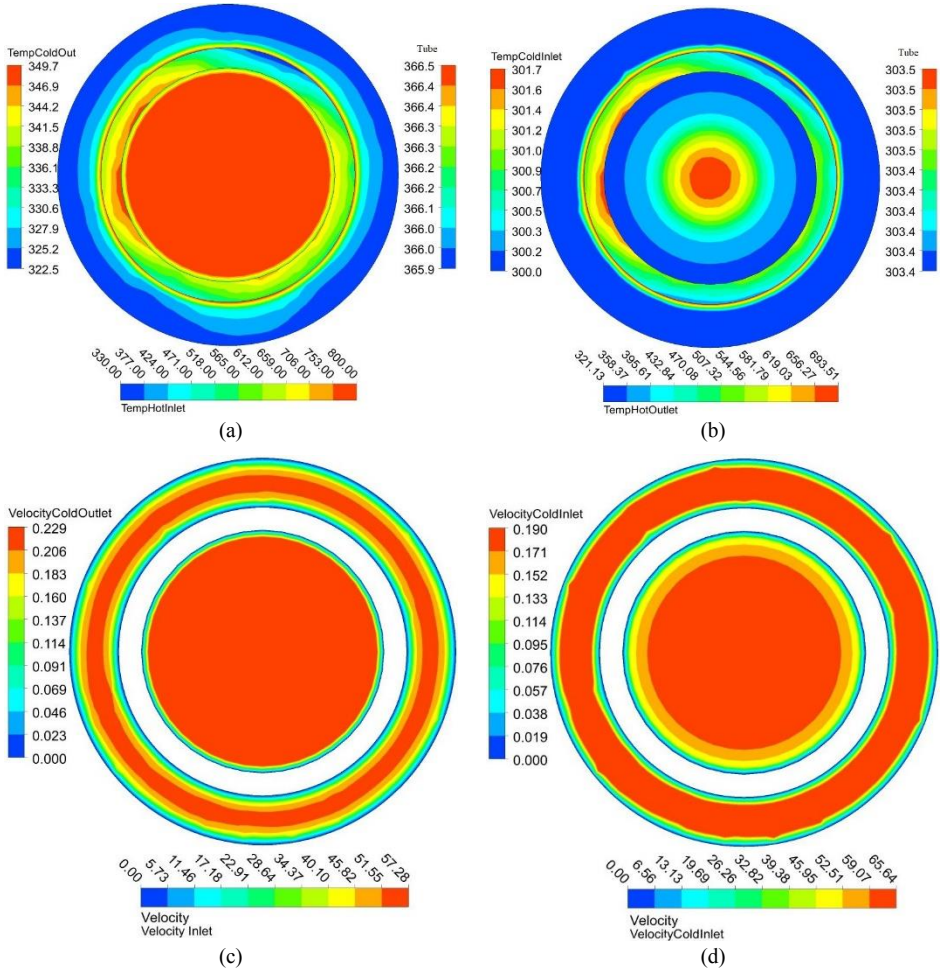

(c) (d)

Fig. 15. Ferrofluid with 4 Vol% and without magnetic field: (a) Temperature (in K) for air inlet and water outlet, (b) Temperature (in K) for air outlet and water inlet, (c) Velocity for air inlet and water outlet, and (d) Velocity for air outlet and water inlet. For $Re_{air} = 42{,}000$ and $Re_{water} = 4500$.

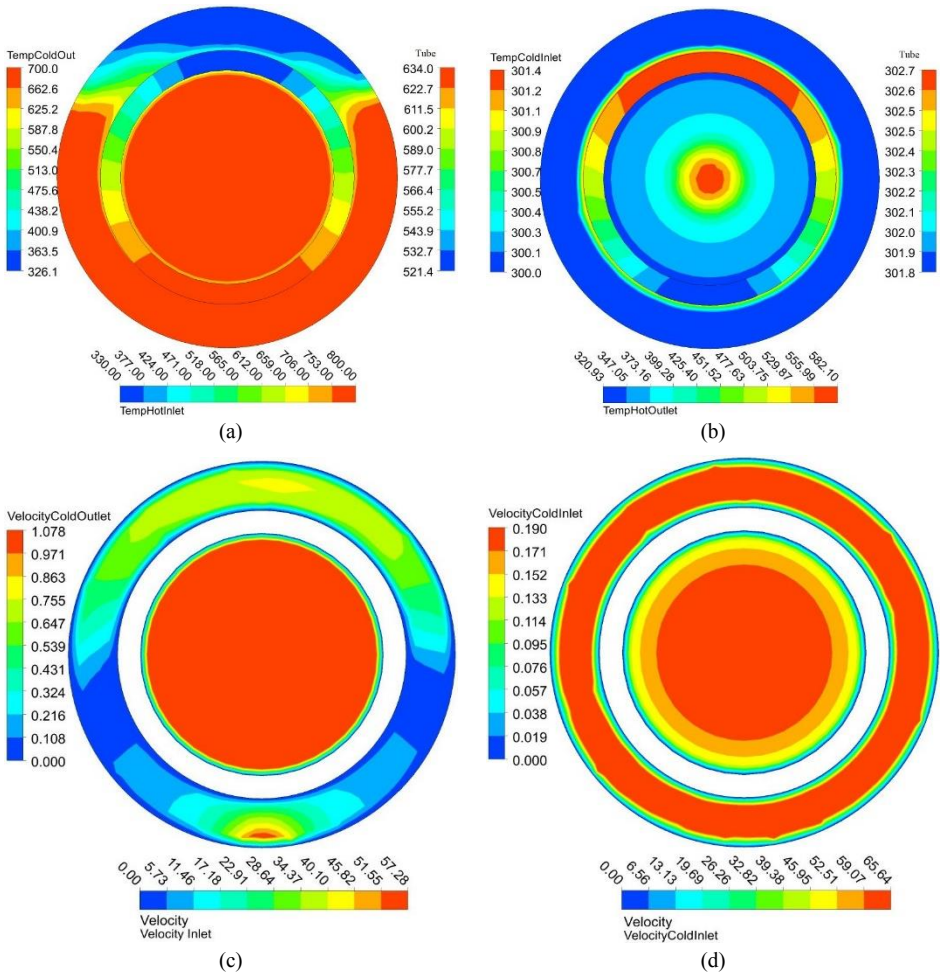

Fig. 16. Ferrofluid with 4 Vol% and with magnetic field of B = 400 G: (a) Temperature (in K) for air inlet and water outlet, (b) Temperature (in K) for air outlet and water inlet, (c) Velocity for air inlet and water outlet, and (d) Velocity for air outlet and water inlet. For $Re_{air} = 42{,}000$ and $Re_{water} = 4500$.

Clear effects of transverse magnetic field on the heat transfer coefficient are shown in Figure 17. According to Figure 17(a), the magnetic field has no effect on the air HTC, which is correct, since no nanoparticles were involved in the air flow. On the contrary, h shows growth with an increase in Reynolds number for ferrofluid, with a bigger effects for B = 400 and 4 vol%. This means that applying magnetic field causes an increase in velocity gradient near the walls, and finally results in enhancing the heat transfer coefficient. Higher HTC for volumetric fraction of 4% is due to its bigger thermal conductivity.

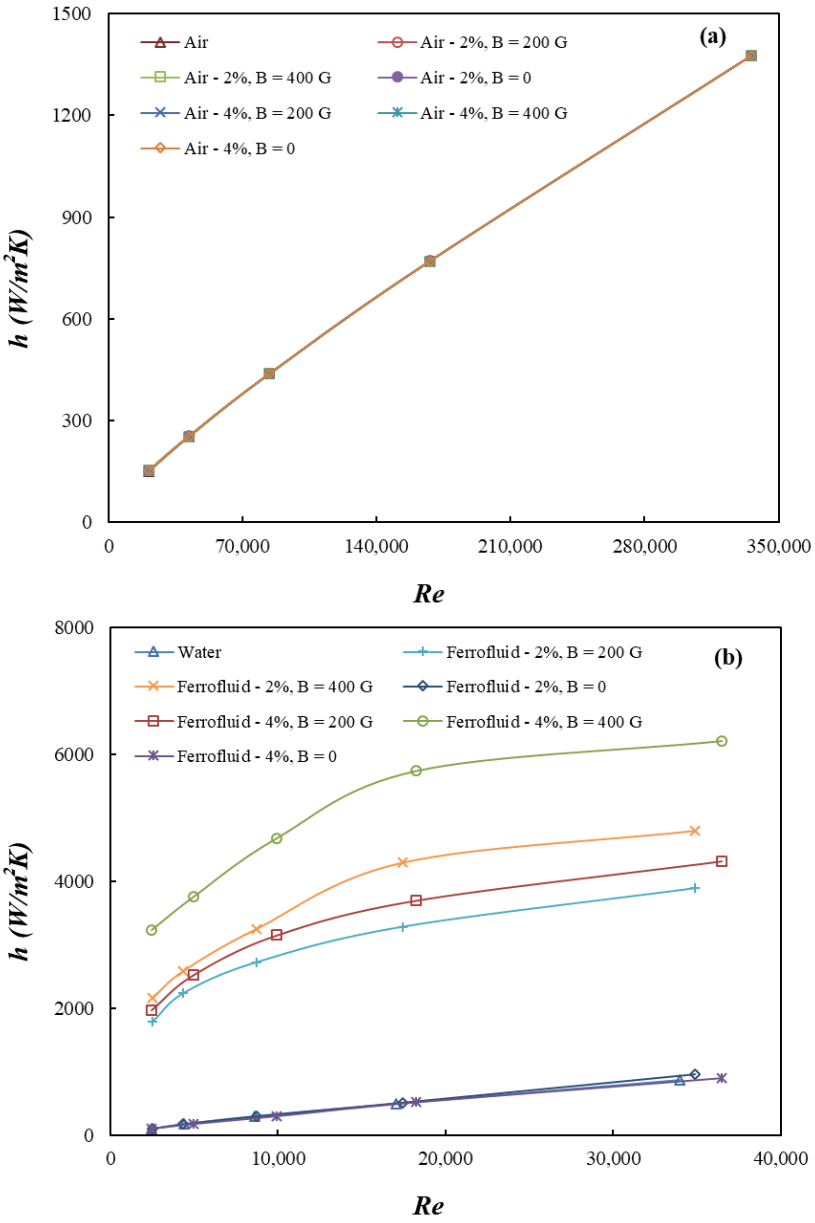

Fig. 17. Effects of magnetic field on the local convective heat transfer coefficient (h): (a) air, (b) ferrofluid.

Figure 18 shows the variation of the pressure drop for air and ferrofluid with different volume fractions, with and without presence of magnetic field. Magnetic field has no effect on the air pressure drop, as it was expected. On the other hand, dispersion of nanoparticles into the base fluid leads to an increase in ferrofluid viscosity. This leads to an increase in pressure drop of ferrofluid with bigger volume fraction. Also, increasing the Reynolds number causes a growth in pressure drop because of high velocity of the ferrofluid for the bigger Reynolds numbers. In addition, as it was shown in Figures 13 to 16, magnetic field cause to an increase in the velocity of the ferrofluid, thus, leads to growth in the pressure drop. This is in accordance with the conclusions presented in [21], [51], [52].

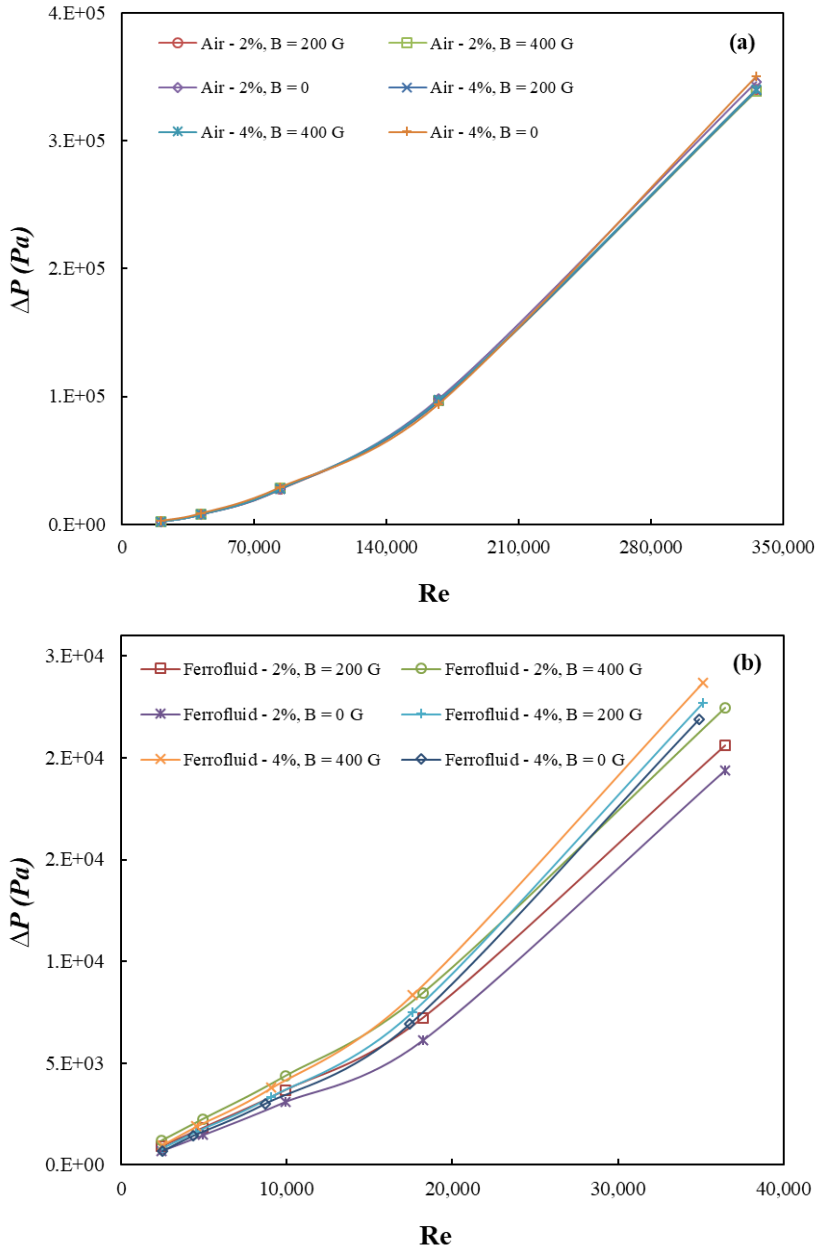

Fig. 18. Magnetic field effects on the pressure drop (f): (a) air tube, (b) ferrofluid tube.

Variation of the friction factor for air and ferrofluid are shown in Figure 19. Similar to the previous figures, ferrofluid results are for different volume fractions and for presence/absence of magnetic field. The friction factor decreases with increasing of the Reynolds number, in all cases. This is due to the fact that the friction factor and velocity have an inverse relationship. Figure 19(b) shows the friction factor increase for the bigger volume fractions and magnetic fields as well.

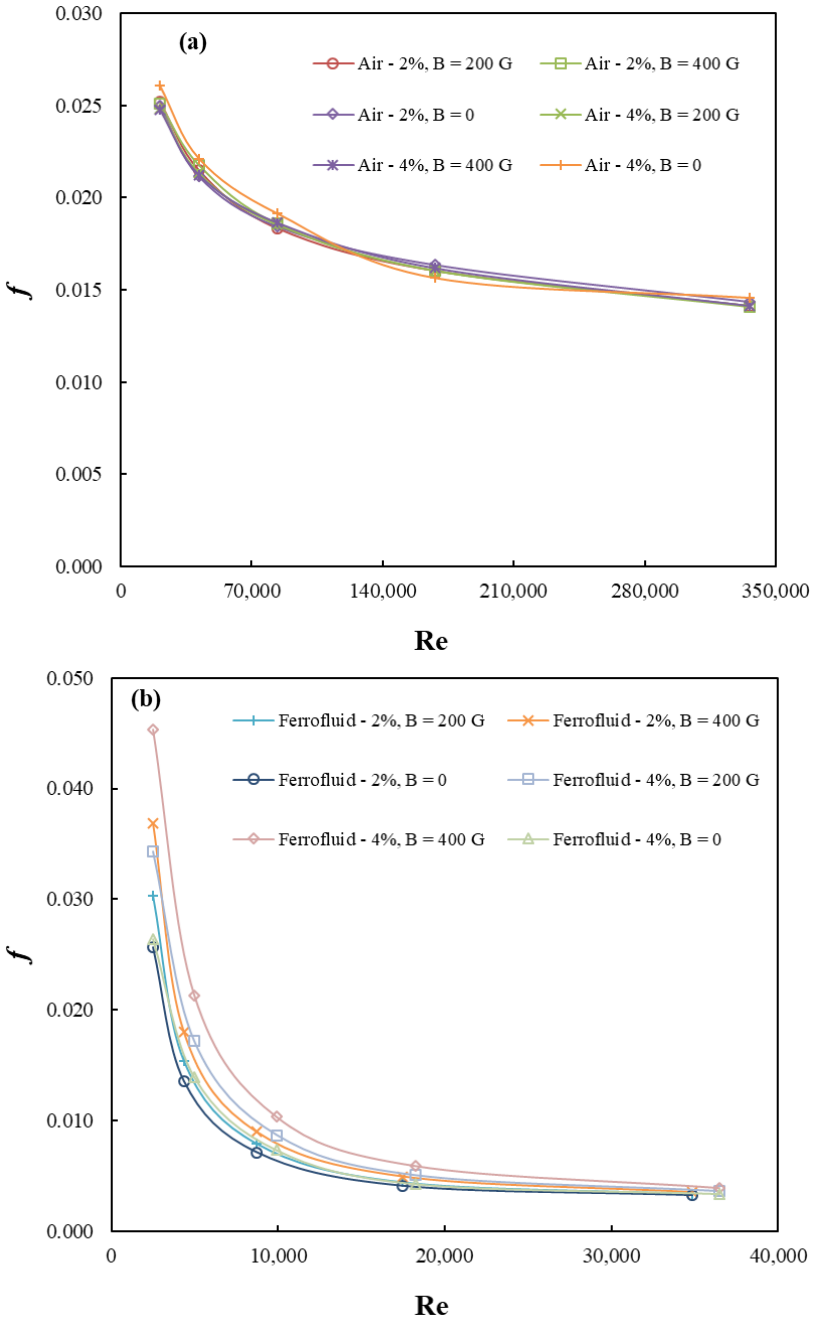

Fig. 19. Effects of magnetic field on the friction factor (f): (a) air tube, (b) ferrofluid tube.

Another important parameter for performance analysis of the heat exchanger is the outlet temperature of both air and ferrofluid/water. As it can be seen from Figure 20(a), the difference between air outlet temperatures for all cases is less than 3%, which means that magnetic field has minimum effect on the air flow characteristics. However, ferrofluid leads to have an increase in the outlet temperature comparing to the base fluid temperature, see Figure 20(b). This is because of higher thermal conductivity of ferrofluids compared to the base fluid, which increases for bigger volumetric fraction and also for bigger magnetic fields. This helps to have higher outlet temperature for the ferrofluid with higher volumetric fraction and bigger magnetic fields.

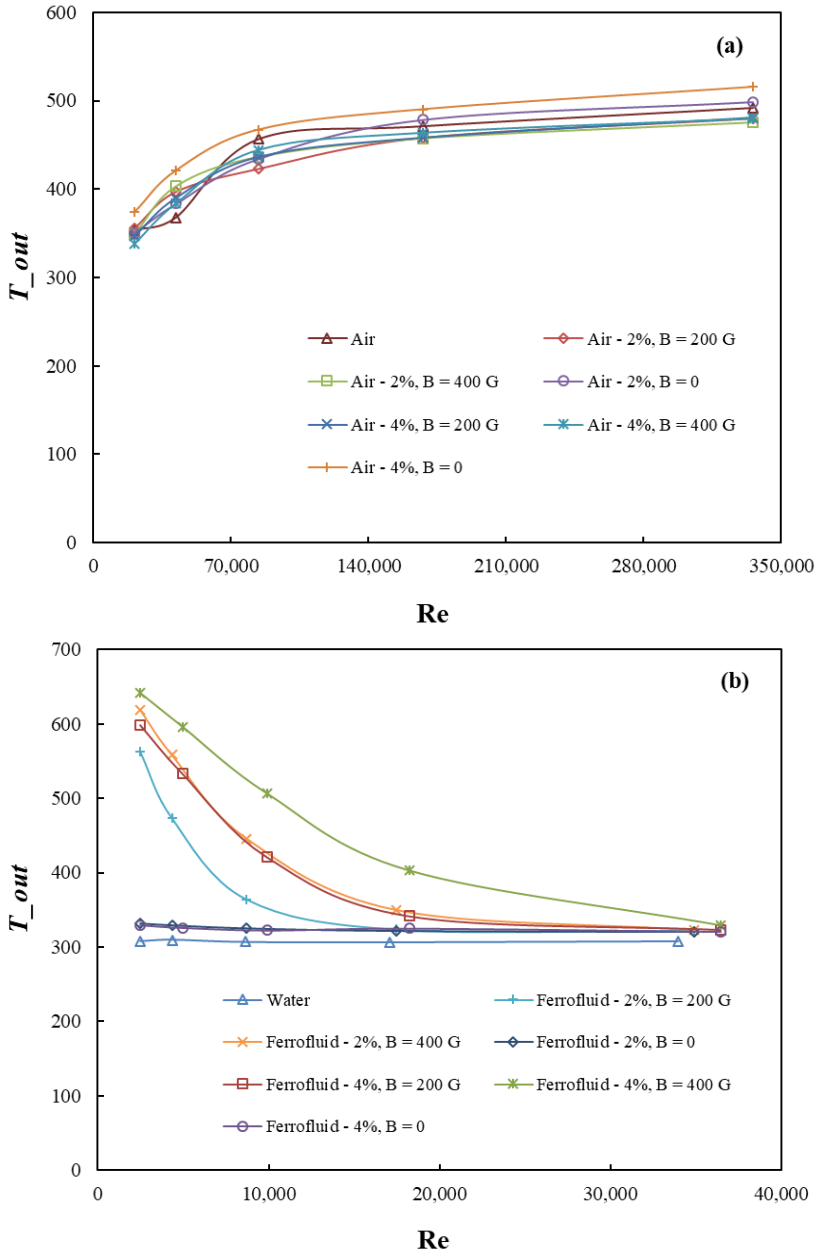

Fig. 20. Thermal efficiency of the current solar collector with different working fluids.

5. Conclusion

In the CAES concept, the air is compressed, stored, and then released through conventional gas turbines. In a diabatic CAES system, the air heat up and is stored as compressed air in a cavern. In this study, a double pipe heat exchanger with Fe_3O_4/water ferrofluid under magnetic field as the secondary fluid is proposed. This secondary fluid absorbs the heat from air and stores in an isolation tank. For this analysis, a transient model was developed in order to obtain boundary conditions for the CFD model and length of the heat exchanger as well. This transient model was fed only with the temperature and pressure at the compressor inlet. A CFD simulation was employed to analyze the proposed heat exchanger before the cavern. Indeed, this method illustrated the effect of magnetic field on the convective heat transfer of ferrofluid. The transient model has shown that the optimum range of temperature and

pressure were from 250 to 1249 K (for temperature) and 80 to 3500 kPa (for pressure). The results demonstrated that increasing the mass flow rate of secondary fluid (water and Fe_3O_4/water nanofluid) decreased the value of cavern temperature. Also, the cavern temperature with the length of 1 m is greater than the other lengths. It means that should be selected more than 1 m for the length of exchanger. The CFD simulation for the double pipe heat exchanger has shown that the magnetic field has the minimum effect on the air flow specifications (the difference between air outlet temperatures for all cases was obtained less than 3%). In addition, using ferrofluid (Fe_3O_4/water nanofluid under magnetic field) as the secondary fluid in the heat exchanger increased the outlet temperature comparing to the base fluid (water). Increasing the volume fraction of nanoparticles in the base fluid increased the convective heat transfer in the heat exchanger. Also, the simulation has illustrated that the pressure drop of ferrofluid was increased by increasing the volume fraction of nanoparticle and magnetic field. A similar conclusion was drawn for the friction factor.

Acknowledgments

The first author acknowledge support from the São Paulo State Research Foundation (FAPESP, Grant no. 2017/20994-1), and second author thanks support of the Brazilian research agency CAPES (Coordination for the Improvement of Higher Education Personnel).

References

[1] A. Khosravi, R. N. N. Koury, L. Machado, and J. J. G. Pabon, "Energy, exergy and economic analysis of a hybrid renewable energy with hydrogen storage system," *Energy*, vol. 148, no. C, pp. 1087–1102, 2018.

[2] A. Khosravi, L. Machado, and R. N. Oliviera, "Time-series prediction of wind speed using machine learning algorithms: A case study Osorio wind farm, Brazil," *Appl. Energy*, vol. 224, no. C, pp. 550–566, 2018.

[3] N. M. Jubeh and Y. S. H. Najjar, "Green solution for power generation by adoption of adiabatic CAES system," *Appl. Therm. Eng.*, vol. 44, pp. 85–89, Nov. 2012.

[4] P. Zhao, J. Wang, Y. Dai, and L. Gao, "Thermodynamic analysis of a hybrid energy system based on CAES system and CO2 transcritical power cycle with LNG cold energy utilization," *Appl. Therm. Eng.*, vol. 91, pp. 718–730, Dec. 2015.

[5] X. Liu, Y. Zhang, J. Shen, S. Yao, and Z. Zhang, "Characteristics of air cooling for cold storage and power recovery of compressed air energy storage (CAES) with inter-cooling," *Appl. Therm. Eng.*, vol. 107, pp. 1–9, Aug. 2016.

[6] Z. Yang, Z. Wang, P. Ran, Z. Li, and W. Ni, "Thermodynamic analysis of a hybrid thermal-compressed air energy storage system for the integration of wind power," *Appl. Therm. Eng.*, vol. 66, no. 1–2, pp. 519–527, May 2014.

[7] H. Lund, G. Salgi, B. Elmegaard, and A. N. Andersen, "Optimal operation strategies of compressed air energy storage (CAES) on electricity spot markets with fluctuating prices," *Appl. Therm. Eng.*, vol. 29, no. 5–6, pp. 799–806, Apr. 2009.

[8] L. Szablowski, P. Krawczyk, K. Badyda, S. Karellas, E. Kakaras, and W. Bujalski, "Energy and exergy analysis of adiabatic compressed air energy storage system," *Energy*, vol. 138, pp. 12–18, 2017.

[9] B. Wang and S. Bauer, "Pressure response of large-scale compressed air energy storage in porous formations," *Energy Procedia*, vol. 125, pp. 588–595, Sep. 2017.

[10] S. Houssainy, M. Janbozorgi, P. Ip, and P. Kavehpour, "Thermodynamic analysis of a high temperature hybrid compressed air energy storage (HTH-CAES) system," *Renew. Energy*, vol. 115, pp. 1043–1054, Jan.

2018.

[11] L. X. Chen, P. Hu, P. P. Zhao, M. N. Xie, D. X. Wang, and F. X. Wang, "A novel throttling strategy for adiabatic compressed air energy storage system based on an ejector," *Energy Convers. Manag.*, vol. 158, pp. 50–59, Feb. 2018.

[12] W. He *et al.*, "Exergy storage of compressed air in cavern and cavern volume estimation of the large-scale compressed air energy storage system," *Appl. Energy*, vol. 208, pp. 745–757, Dec. 2017.

[13] Y. Huang *et al.*, "Techno-economic Modelling of Large Scale Compressed Air Energy Storage Systems," *Energy Procedia*, vol. 105, pp. 4034–4039, May 2017.

[14] Y. Mazloum, H. Sayah, and M. Nemer, "Exergy analysis and exergoeconomic optimization of a constant-pressure adiabatic compressed air energy storage system," *J. Energy Storage*, vol. 14, pp. 192–202, Dec. 2017.

[15] M. J. Kim and T. S. Kim, "Feasibility study on the influence of steam injection in the compressed air energy storage system," *Energy*, vol. 141, pp. 239–249, Dec. 2017.

[16] A. H. Alami, K. Aokal, J. Abed, and M. Alhemyari, "Low pressure, modular compressed air energy storage (CAES) system for wind energy storage applications," *Renew. Energy*, vol. 106, pp. 201–211, Jun. 2017.

[17] H. Meng, M. Wang, M. Aneke, X. Luo, O. Olumayegun, and X. Liu, "Technical performance analysis and economic evaluation of a compressed air energy storage system integrated with an organic Rankine cycle," *Fuel*, vol. 211, pp. 318–330, Jan. 2018.

[18] M. Malekan and A. Khosravi, "Investigation of convective heat transfer of ferrofluid using CFD simulation and adaptive neuro-fuzzy inference system optimized with particle swarm optimization algorithm," *Powder Technol.*, vol. 333, pp. 364–376, 2018.

[19] S. V. Mousavi, M. Sheikholeslami, M. Gorji bandpy, and M. Barzegar Gerdroodbary, "The Influence of magnetic field on heat transfer of magnetic nanofluid in a sinusoidal double pipe heat exchanger," *Chem. Eng. Res. Des.*, vol. 113, pp. 112–124, 2016.

[20] P. Naphon and S. Wiriyasart, "Experimental study on laminar pulsating flow and heat transfer of nanofluids in micro-fins tube with magnetic fields," *Int. J. Heat Mass Transf.*, vol. 118, pp. 297–303, Mar. 2018.

[21] S. Ahangar Zonouzi *et al.*, "Experimental investigation of the flow and heat transfer of magnetic nanofluid in a vertical tube in the presence of magnetic quadrupole field," *Exp. Therm. Fluid Sci.*, vol. 91, 2018.

[22] M. Rahimi-Gorji, O. Pourmehran, M. Gorji-Bandpy, and D. D. Ganji, "Unsteady squeezing nanofluid simulation and investigation of its effect on important heat transfer parameters in presence of magnetic field," *J. Taiwan Inst. Chem. Eng.*, vol. 67, pp. 467–475, 2016.

[23] M. Rahimi-Gorji, O. Pourmehran, M. Gorji-Bandpy, and T. B. Gorji, "CFD simulation of airflow behavior and particle transport and deposition in different breathing conditions through the realistic model of human airways," *J. Mol. Liq.*, vol. 209, pp. 121–133, 2015.

[24] M. Rahimi-Gorji, T. B. Gorji, and M. Gorji-Bandpy, "Details of regional particle deposition and airflow structures in a realistic model of human tracheobronchial airways: Two-phase flow simulation," *Comput. Biol. Med.*, vol. 74, pp. 1–17, 2016.

[25] M. Sheikholeslami, S. A. Shehzad, and Z. Li, "Nanofluid heat transfer intensification in a permeable channel due to magnetic field using lattice Boltzmann method," *Phys. B Condens. Matter*, vol. 542, pp. 51–58, Aug. 2018.

[26] N. Gan Jia Gui, C. Stanley, N.-T. Nguyen, and G. Rosengarten, "Ferrofluids for heat transfer enhancement under an external magnetic field," *Int. J. Heat Mass Transf.*, vol. 123, pp. 110–121, Aug. 2018.

[27] S. R. Hosseini, M. Sheikholeslami, M. Ghasemian, and D. D. Ganji, "Nanofluid heat transfer analysis in a microchannel heat sink (MCHS) under the effect of magnetic field by means of KKL model," *Powder*

Technol., vol. 324, pp. 36–47, Jan. 2018.

[28] P. Naphon and S. Wiriyasart, "Pulsating flow and magnetic field effects on the convective heat transfer of TiO2-water nanofluids in helically corrugated tube," *Int. J. Heat Mass Transf.*, vol. 125, pp. 1054–1060, Oct. 2018.

[29] N. Sandeep and I. L. Animasaun, "Heat transfer in wall jet flow of magnetic-nanofluids with variable magnetic field," *Alexandria Eng. J.*, vol. 56, no. 2, pp. 263–269, Jun. 2017.

[30] N. Hatami, A. Kazemnejad Banari, A. Malekzadeh, and A. R. Pouranfard, "The effect of magnetic field on nanofluids heat transfer through a uniformly heated horizontal tube," *Phys. Lett. Sect. A Gen. At. Solid State Phys.*, vol. 381, no. 5, pp. 510–515, 2017.

[31] L. Sha, Y. Ju, H. Zhang, and H. Z. Lili Sha, Yonglin Ju, "The influence of the magnetic field on the convective heat transfer characteristics of Fe3O4/water nanofluids," *Appl. Therm. Eng.*, vol. 126, pp. 108–116, 2017.

[32] S. Hariri, M. Mokhtari, M. B. Gerdroodbary, and K. Fallah, "Numerical investigation of the heat transfer of a ferrofluid inside a tube in the presence of a non-uniform magnetic field," *Eur. Phys. J. Plus*, vol. 132, no. 2, pp. 1–14, 2017.

[33] M. Mokhtari, S. Hariri, M. Barzegar Gerdroodbary, and R. Yeganeh, "Effect of non-uniform magnetic field on heat transfer of swirling ferrofluid flow inside tube with twisted tapes," *Chem. Eng. Process. Process Intensif.*, vol. 117, no. March, pp. 70–79, 2017.

[34] A. Khosravi and M. Malekan, "Effect of Magnetic Field on Heat Transfer Coefficient of Fe3O4-Water Ferrofluid Using Artificial Intelligence and CFD simulation," *Eur. Phys. J. Plus (under Rev.*, 2018.

[35] A. Khosravi, M. Malekan, and M. E. H. Assad, "Numerical analysis of magnetic field effects on the heat transfer enhancement in ferrofluids for a parabolic trough solar collector," *Renew. Energy (under Rev.*, 2018.

[36] M. Sheikholeslami, M. Barzegar Gerdroodbary, S. V. Mousavi, D. D. Ganji, and R. Moradi, "Heat transfer enhancement of ferrofluid inside an 90° elbow channel by non-uniform magnetic field," *J. Magn. Magn. Mater.*, vol. 460, pp. 302–311, Aug. 2018.

[37] H.-M. Kim, J. Rutqvist, D.-W. Ryu, B.-H. Choi, C. Sunwoo, and W.-K. Song, "Exploring the concept of compressed air energy storage (CAES) in lined rock caverns at shallow depth: A modeling study of air tightness and energy balance," *Appl. Energy*, vol. 92, pp. 653–667, Apr. 2012.

[38] R. Hamilton and O. Crosser, "Thermal conductivity of heterogeneous two-component systems," *Ind. Eng. Chem. Fundam.*, vol. 1, no. 3, pp. 187–191, 1962.

[39] E. Shojaeizadeh, F. Veysi, and A. Kamandi, "Exergy efficiency investigation and optimization of an Al2O3-water nanofluid based flat-plate solar collector," *Energy Build*, vol. 101, pp. 12–23, 2015.

[40] A. Khosravi, R. N. N. Koury, and L. Machado, "Thermo-economic analysis and sizing of the components of an ejector expansion refrigeration system," *Int. J. Refrig.*, vol. 86, pp. 463–479, Feb. .

[41] E. Bellos, C. Tzivanidis, and D. Tsimpoukis, "Thermal enhancement of parabolic trough collector with internally finned absorbers," *Sol. Energy*, vol. 157, no. July, pp. 514–531, 2017.

[42] B. S. Petukhov, "Heat transfer in turbulent pipe flow with variable physical properties," *Harnett JP, Ed. Adv. heat Transf.*, vol. 6, pp. 504–564, 1970.

[43] R. N. Faria, R. O. Nunes, R. N. N. Koury, and L. Machado, "Dynamic modeling study for a solar evaporator with expansion valve assembly of a transcritical CO2 heat pump," *Int. J. Refrig.*, vol. 64, pp. 203–213, 2016.

[44] T. L. Bergman, A. S. Lavine, F. P. Incropera, and D. P. DeWitt, *Fundamentals of Heat and Mass Transfer*, 7th ed. John Wiley & Sons, 2011.

[45] J. Garcia, T. Ali, W. M. Duarte, A. Khosravi, and L. Machado, “Comparison of transient response of an evaporator model for water refrigeration system working with R1234yf as a drop-in replacement for R134a,” *Int. J. Refrig.*, 2018.

[46] L. Machado, P. Haberschill, and M. Lallemand, “Masse du fluide frigorigène dans un évaporateur en fonctionnement permanent ou transitoire: Refrigerant mass inside an evaporator in a steady or non-steady state,” *Int. J. Refrig.*, vol. 21, no. 6, pp. 430–439, Sep. 1998.

[47] R. Vi. De Melo Reis, R. N. Oliviera, L. Machado, and R. N. N. Koury, “Using a heat pump as an alternative to support solar collector for water heating in Brazil,” *Int. J. Air-Conditioning Refrig.*, vol. 20, no. 03, p. 1250013, 2012.

[48] R. N. de Oliveira, R. N. Faria, F. Antonanzas-Torres, L. Machado, and R. N. N. Koury, “Dynamic model and experimental validation for a gas cooler of a CO_2 heat pump for heating residential water,” *Sci. Technol. Built Environ.*, vol. 22, no. 1, pp. 30–40, Jan. 2016.

[49] R. V. De Melo Reis, R. N. Oliveira, L. Machado, and R. N. N. Koury, “Using a heat pump as an alternative to support solar collector for water heating in Brazil,” *Int. J. Air-Conditioning Refrig.*, vol. 20, no. 03, p. 1250013, Sep. 2012.

[50] B. Zheng, C. X. Lin, and M. A. Ebadian, “Combined turbulent forced convection and thermal radiation in a curved pipe with uniform wall temperature,” *Numer. Heat Transf. A Appl.*, vol. 44, pp. 149–167, 2003.

[51] R. Azizian, E. Doroodchi, T. McKrell, J. Buongiorno, L. W. Hu, and B. Moghtaderi, “Effect of magnetic field on laminar convective heat transfer of magnetite nanofluids,” *Int. J. Heat Mass Transf.*, vol. 68, pp. 94–109, 2014.

[52] M. Amani, M. Ameri, and A. Kasaeian, “The Experimental Study of Convection Heat Transfer Characteristics and Pressure Drop of Magnetite Nanofluid in a Porous Metal Foam Tube,” *Transp. Porous Media*, vol. 116, no. 2, pp. 959–974, 2017.